Enhancing electrocatalytic hydrogen evolution of MoS$_2$ enabled by electrochemical cation implantation for simultaneous surface-defect and phase engineering

Mun Kyoung Kim [a], Bipin Lamichhane [b], Byunggon Song [a], Sunhyeong Kwon [a], Benzhi Wang [a], Shyam Kattel [b,*], Ji Hoon Lee [c,*], Hyung Mo Jeong [a,*]

[a] School of Mechanical Engineering and Department of Smart Fab. Technology, Sungkyunkwan University, 2066 Seobu-ro, Suwon 16419, the Republic of Korea
[b] Department of Physics, Florida A&M University, Tallahassee, FL 32307, United States
[c] School of Materials Science and Engineering and KNU Advanced Material Research Institute, Kyungpook National University, 80 Daehak-ro, Buk-gu, Daegu 41566, the epublic of Korea

ARTICLE INFO

ABSTRACT

The increasing demand for energy-efficient and cost-effective water-splitting systems has prompted research on non-precious-metal-based electrocatalysts for the hydrogen evolution reaction (HER) over a wide pH range. Molybdenum sulfide (MoS$_2$) has received considerable attention owing to its excellent HER activity in acidic media. However, its competitive HER properties must be improved to achieve better performance in alkaline or neutral environments. In this study, we introduced an electrochemical cation implantation (ECI) process as a versatile method to enhance the electrocatalytic properties of MoS$_2$. By modifying the microstructure of MoS$_2$, the ECI process induced vacancies in Mo and S, primarily in the basal planes and facilitated a gradual transition from the semiconducting (2H) to metallic (1T) phase. The optimized ECI-processed MoS$_2$ catalysts exhibited improved HER activities and low overpotentials (η_{10}, 144 mV) over the entire pH range compared with bare MoS$_2$ catalysts, highlighting the potential application of the ECI process for enhanced electrocatalysts.

1. Introduction

The combustion of fossil fuels has resulted in a continuous increase in CO$_2$ emissions, causing environmental problems [1,2]. Although various technologies such as CO$_2$ capture and sequestration [3,4] and electrochemical CO$_2$ transformation have been proposed to address these issues [5], the dependence on fossil fuels continues to increase [6,7]. Therefore, H$_2$ has gained significant attention as an alternative energy carrier because its high gravimetric energy density (approximately 120 MJ kg^{-1}) outperforms its current carbon-based counterparts (45–55 MJ kg^{-1}) [8]. In this regard, water (H$_2$O) electrolysis [9,10] coupled with renewable energy resources is considered a viable solution because it can produce H$_2$ via electrochemical reactions on the cathode. The cathodic reaction, also referred to as the hydrogen evolution reaction (HER), is facilitated by Pt-based precious metal groups; however, their limited availability hinders the widespread propagation of water electrolysis in practical applications. Therefore, it is desirable to develop cost-effective catalysts and enhance the electrocatalytic performance of conventional catalysts using simple and controllable processes.

Various alternative catalysts, such as N-/S-/B-doped carbonaceous catalysts, transition metal-based carbide/nitride/phosphide/sulfide catalysts, and Pt-modified catalysts, have been extensively studied as potential replacements for Pt-based catalysts [11–13]. Among these, molybdenum disulfide (MoS$_2$), one of the most widely studied two-dimensional transition metal dichalcogenides, has been considered a promising alternative owing to its prolific properties, including earth-abundance, tunable band gap, high electrical conductivity, and electron mobility, that fulfill the requirements for replacing Pt-based catalysts [14–16]. However, satisfactory HER activity has not been achieved with bulk MoS$_2$ catalysts because of the large proportion of catalytically inert basal planes that originate from their crystallographic features. Previous studies have demonstrated intrinsic and extrinsic improvements in electrocatalytic activity primarily by (1) phase engineering [17–20] to adjust the electrical conductivity (semiconducting 2H phase vs. metallic 1T phase); (2) aliovalent element doping [21–26] to modify the catalytic active sites; and (3) post-chemical treatments

---

such as plasma treatment [27,28] and chemical etching [29,30] to introduce vacancies (mainly, S vacancies) and cracks as an additional active sites, respectively. However, despite previous studies demonstrating improved performance only under specific pH conditions, it is essential to further investigate these outcomes over a wide pH range for industrial applications [31,32]. This is attributed to the fact that high HER activities in electrolytes under different pH conditions require entirely different approaches for the development of catalyst materials and their corresponding properties. Furthermore, previously adopted synthetic processes [17–30,33–38] are relatively complex, which make it difficult to control the defect amounts and the crystal structure of the treated catalysts. Consequently, it is challenging to determine whether these methods improve the activities intrinsically or extrinsically [39]. To address this issue, it is essential to develop approaches that can populate the inherent active sites in MoS_2 catalysts with catalytically favorable phases.

In this study, we demonstrated a simple, facile, and precisely controllable electrochemical cation implantation (ECI) process that enhanced the catalytic activity of the MoS_2 catalyst for the HER process by engineering its phase (2H → 1T) and making its basal planes rich in Mo- and S-vacancies (V_{Mo} and V_S) [40]. The combined analyses of X-ray diffraction (XRD), transmission electron microscopy (TEM), Raman spectroscopy, and in situ and ex situ X-ray absorption fine structure (XAFS) spectroscopy, and density functional theory calculations systematically characterized the progress of phase transition and vacancy formation during the ECI process, elucidating their roles in facilitating the HER. The optimally tuned MoS_2 catalysts grown on carbon cloth exhibited significantly enhanced HER performance under universal pH conditions compared with the bulk MoS_2 catalysts, as evidenced by the low overpotential at a current density of 10 mA cm^{-2} (η_{10}, 144, 184, and 212 mV for acid, base, and neutral electrolytes, respectively) and superior Tafel slopes (81, 92, and 133 mV dec^{-1} for acid, base, and neutral electrolytes, respectively).

2. Experimental section

2.1. Materials and chemicals

All chemicals were obtained from commercial sources and used as received, unless otherwise stated. Ammonium molybdate tetrahydrate [$(NH_4)_6Mo_7O_{24}\bullet4$ H_2O] and thiourea (CH_4N_2S) were purchased from Alfa Asar. Carbon cloth was purchased from the Fuel Cell Store. MoS_2 (nanopowder, 90 nm diameter, 99% trace metals basis), poly(vinylidene fluoride) (PVDF, average M_w of approximately 534000 by gel permeation chromatography, powder form), N-methyl-2-pyrrolidinone (NMP, 99%), acetic acid (glacial, $\geq$ 99%), sulfuric acid (H_2SO_4, 95.0–98.0%) and nitric acid (HNO_3, 70%) were purchased from Sigma-Aldrich. Lithium hexafluorophosphate ($LiPF_6$) in ethyl carbonate/diethyl carbonate (EC/DEC = 1:1, v/v) and sodium hexafluorophosphate ($NaPF_6$) in EC/DEC (1:1, v/v) were purchased from Wellcos Corp. Deionized (DI) water and acetone were purchased from Daejung.

2.2. Synthesis of 2H MoS_2 catalysts on carbon cloth

Carbon cloths (1 × 2 cm^2) were sequentially and thoroughly washed with acetone, ethanol, and DI water via sonication for 20 min to remove organics and impurities. Subsequently, the washed carbon cloth was immersed in a mixture of H_2SO_4 and HNO_3 solutions (volume ratio of 1:3) overnight.

Ammonium molybdate tetrahydrate (0.206 g) and thiourea (0.3806 g) were dissolved in DI water (30 mL) under vigorous stirring to form a homogeneous solution. The solution was then transferred to a 50-mL Teflon-lined stainless-steel autoclave, followed by the addition of the aforementioned carbon cloth. The autoclave reactor was maintained at 220 °C for 18 h, and then cooled to room temperature. The product was thoroughly washed with DI water and ethanol and dried at 60 °C under

vacuum for further electrochemical characterization as the working electrode.

2.3. ECI process on 2H MoS_2

An ECI process was conducted on 2H MoS_2 catalysts grown on a carbon cloth, which was used as the working electrode, to engineer phase transition and vacancy formation. The working electrode was assembled into a 2032-type coin cell in which Li foil and a porous polypropylene membrane (Celgard 2400) served as the counter/reference electrode and separator, respectively. A cosolvent of EC/DEC containing $LiPF_6$ (1.0 M) was used as the electrolyte.

The assembled coin cell was discharged to selected voltages (1.0, 0.7, 0.2, and 0.0 V vs. Li/Li$^+$) at a current density of –100 µA cm^{-2} for a controlled ECI process. Upon completion of the discharging process, the coin cell was disassembled to retrieve the working electrodes, followed by sequential and thorough washing with acetone, DI water, and a 1.0 mM acetic acid solution several times. The washed MoS_2 electrode was collected and dried in a vacuum oven at 60 °C for 6 h.

To test the universality of our ECI process, we also applied it to tungsten disulfide (WS_2). All procedures were identical, except that the working electrode was prepared using a slurry containing commercial WS_2 powder and a polymer binder (polyvinylidene difluoride). Additionally, a similar ECI process was conducted using sodium (Na) ions as the cation carrier. All procedures remained the same as described above, except that Na metal was used as the counter/reference electrode and a cosolvent of EC/DEC containing $NaPF_6$ (1.0 M) was used as the electrolyte.

2.4. Materials characterization

The crystal structures of the prepared samples were characterized using XRD (MiniFlex 600, Rigaku). The chemical states were investigated using X-ray photoelectron spectroscopy (XPS; K-alpha$^+$, Thermo Scientific). The working electrode was weighed by using a micro-balance (XPR26CV, readability = 1 µg, Mettler Toledo). Raman spectra were recorded using Raman spectroscopy (XperRam S, Nano-base) equipped with a 532-nm excitation laser at 25 °C. The morphological and structural changes were observed using field-emission scanning electron microscopy (SUPRA55VP, Carl Zeiss) and field-emission transmission electron microscopy (JEM-2100 F, JEOL). Electron spin resonance (ESR, JES-X320, JEOL) spectroscopy was conducted at 25 °C to evaluate the concentration of vacancies by unpaired electrons. Elemental analysis of Mo and S were performed by inductively coupled plasma optical spectroscopy (ICP-OES, Agilent 5100, Agilent).

2.5. Evaluation of electrocatalytic HER performance

The electrocatalytic H_2 production was performed using a potentiostat (VMP3, Biologic) in a three-electrode configuration. A reversible hydrogen electrode (HydroFlex, ET-070, EDAQ) and graphite rod served as the reference and counter electrodes, respectively. HER tests were performed in 0.5 M sulfuric acid (H_2SO_4), 1.0 M potassium hydroxide (KOH), and 1.0 M phosphate buffer solution (PBS) by linear sweep voltammetry (LSV) at a scan rate of 5 mV s^{-1}. Stability tests were conducted under cyclic voltammetry (CV) mode at a scan rate of 50 mV s^{-1} for 1000 cycles from 0–0.3 V vs. RHE (here and afterward, V_{RHE}). To obtain the solution resistance in the Nyquist plot, electrochemical impedance spectroscopy analysis was performed at a potential of –0.2 V_{RHE} in the frequency range of 0.1 Hz to 1 MHz with an AC amplitude of 5 mV. The electrode potential was controlled using an iR compensation (85%). The electrochemical active surface area (ECSA) was calculated using the electrochemical double-layer capacitance (C_{dl}) method. The CV technique was conducted in the non-Faradaic potential window of 0.4–0.5 V_{RHE} with increasing scan rates. ECSA was evaluated by dividing the specific capacitance (C_s = 0.040 mF cm^{-2} for MoS_2) [41,

42]. Long-term stability tests were performed by chronopotentiometry (CP) at a current density of –10 mA cm^{-2} for 100 h.

2.6. XAFS analyses

XAFS analyses were performed to identify the local physicochemical structural evolution of Mo in MoS$_2$ with different degrees of lithiation at the 10 C beamline (Wide XAFS) of the Pohang Light Source-II (PLS-II) at the Pohang Accelerator Laboratory (PAL), Republic of Korea. The storage ring was operated in the top-up mode at an energy of 3.0 GeV and operating current of 300 mA. The XAFS spectra at the Mo K-edge (20 keV) were obtained in the transmission mode. Each spectrum was calibrated using the edge energy (E$_0$) of the Mo foil, which was recorded simultaneously. The ATHENA and ARTEMIS software included in the IFFEFIT package were used to analyze the X-ray absorption near edge structure (XANES) and extended X-ray absorption fine structure (EXAFS) profiles. The detailed procedure reported by Ravel et al. was followed during data processing [43]. The EXAFS spectrum (χ(k)) was weighted with the k^3 value to intensify the signal in the high k-regime. A Hanning window function was used for the Fourier transform. All EXAFS fittings were performed in R-space; the data are summarized in Figures S1, S13, **and** S14 and Tables S2–S8, S13, **and** S14.

A lab-made acrylic kit was used for the in situ XAFS analyses [44]. The areal loading of the pristine 2H and ECI-processed MoS$_2$ electrodes was controlled at approximately 1.0 mg$_{MoS2}$ cm^{-2} to achieve sufficient XAFS signal. The other conditions were the same as those used for electrochemical measurements. Transmission and fluorescence signals were detected. Each target potential was maintained using chronoamperometry for 15 min to reach the equilibrium potential of the working electrode before the XAFS measurements and for an additional 25 min during the XAFS measurement.

2.7. Computational methods

The spin-polarized density functional theory (DFT) [45] calculations were performed using the Vienna ab initio simulation package (VASP) [46,47] code. The exchange and correlation effects were accounted for using Perdew-Burke-Ernzerhof (PBE) [48] functionals within the generalized gradient approximation. The projected augmented plane wave (PAW) [49] method was used to describe the electron-ion interaction. We used the DFT-D3 method proposed by Grimme et al. [50] to correct Van der Waal's interaction. A kinetic energy cutoff of 450 eV was used for all the calculations.

Previous experimental and DFT results have reported five different structures of MoS$_2$, namely, 2H MoS$_2$, 1T MoS$_2$, 1T\` MoS$_2$, 1T\`\` MoS$_2$, and 1T\`\`\` MoS$_2$ [51–53]. Similar to the previous DFT approach [52,54], a monolayer slab of 5 × 5 × 1 and 2 × 2 × 1 were used to represent the surfaces of 2H/1T and 1T\`/1T\`\`/1T\`\`\` MoS$_2$, respectively. Even though the supercell meshes (5 × 5 × 1 *vs.* 2 × 2 × 1) of the surface slab are different, we maintained a S-vacancy concentration of ~3% on all surface slabs. The artificial interactions between the slab and its periodic images were minimized by adding a vacuum of 18 Å perpendicular to the slab. A Monkhorst [55] k-points mesh of 2 × 2 × 1 and 4 × 4 × 1 was used for the slab of 5 × 5 × 1and 2 × 2 × 1, respectively. Optimized geometry was obtained when the Hellmann-Feynman force on each ion was smaller than 0.02 eV Å^{-1}.

Hydrogen binding energy (BE) was calculated as

BE(hydrogen) = E(slab+hydrogen) – E(slab) – E(hydrogen),

where E(slab+hydrogen), E(slab), and E(hydrogen) are the total energies of the slab with hydrogen, pristine slab, and hydrogen in the gas phase, respectively.

Using the computational hydrogen electrode model [56] developed by Nørskov and coworkers, the change in Gibbs free energy is calculated as:

$$\Delta G = \Delta E + \Delta ZPE - T\Delta S,$$

where ΔE is the change in energy of a reaction step that can be obtained from DFT calculations, ΔZPE and $T\Delta S$ are the zero-point and entropy contribution to free energy, respectively, and T is 298.15 K. The energy barriers for H$_2$O dissociation were calculated using the climbing image nudged elastic band (CI-NEB) method [57].

3. Results and discussion

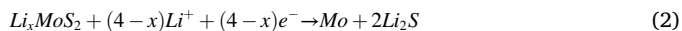### 3.1. Phase and defects engineering on MoS$_2$ via the ECI process

Phase- and defect-engineered MoS$_2$ electrocatalysts were successfully synthesized using ECI. Pristine 2H MoS$_2$ was fabricated as the electrode for a 2032-type coin cell. Thereafter, the ECI process was performed by discharging the pristine 2H MoS$_2$ catalysts to the designated voltages using a high-resolution potentiostat (see the detailed voltage conditions in the Experimental Section 2.3).

Fig. 1a illustrates the stepwise ECI process and the corresponding phase and defect engineering of the MoS$_2$ catalysts. It is well established that Li ions can reduce electrode materials, such that desirable physicochemical properties can be achieved by applying an appropriate electrochemical potential [58,59]. First, we monitored the phase transition of 2H MoS$_2$ (semiconducting) to 1T MoS$_2$ (metallic), followed by the formation of vacancies using high-resolution TEM (HRTEM) analyses. Li ions were intercalated into the interlayer galleries of 2H MoS$_2$ (denoted as pristine 2H MoS$_2$), yielding 1T MoS$_2$ at approximately 1.1 V vs. Li/Li$^+$ (Eq. (1)) [60,61].

$$MoS_2 + xLi^+ + xe^- \rightarrow Li_xMoS_2 \tag{1}$$

The fast Fourier transform (FFT) patterns viewed along the [001] direction exhibiting six-fold symmetry, gradually lost their original contrast, suggesting the formation of vacancies in 1T MoS$_2$. Upon entry into this voltage range, pristine 2H MoS$_2$ partially transformed into 1T MoS$_2$ to form a mixed phase (denoted as p-2H/1T MoS$_2$), which may have resulted from the presence of a two-phase region of pristine 2H MoS$_2$ and lithiated MoS$_2$ domains. The deeper ECI process, in turn, yielded vacancy-rich 1T MoS$_2$ (denoted as vr-1T MoS$_2$) because the lattice fringes became less distinguishable, while vr-1T MoS$_2$ maintained its original six-fold symmetry in the FFT pattern (Fig. 1b). The plate-like particle morphology in the high-resolution SEM (HRSEM) image suggests the formation of vacancy on the vr-1T MoS$_2$ surface (Fig. 1c).
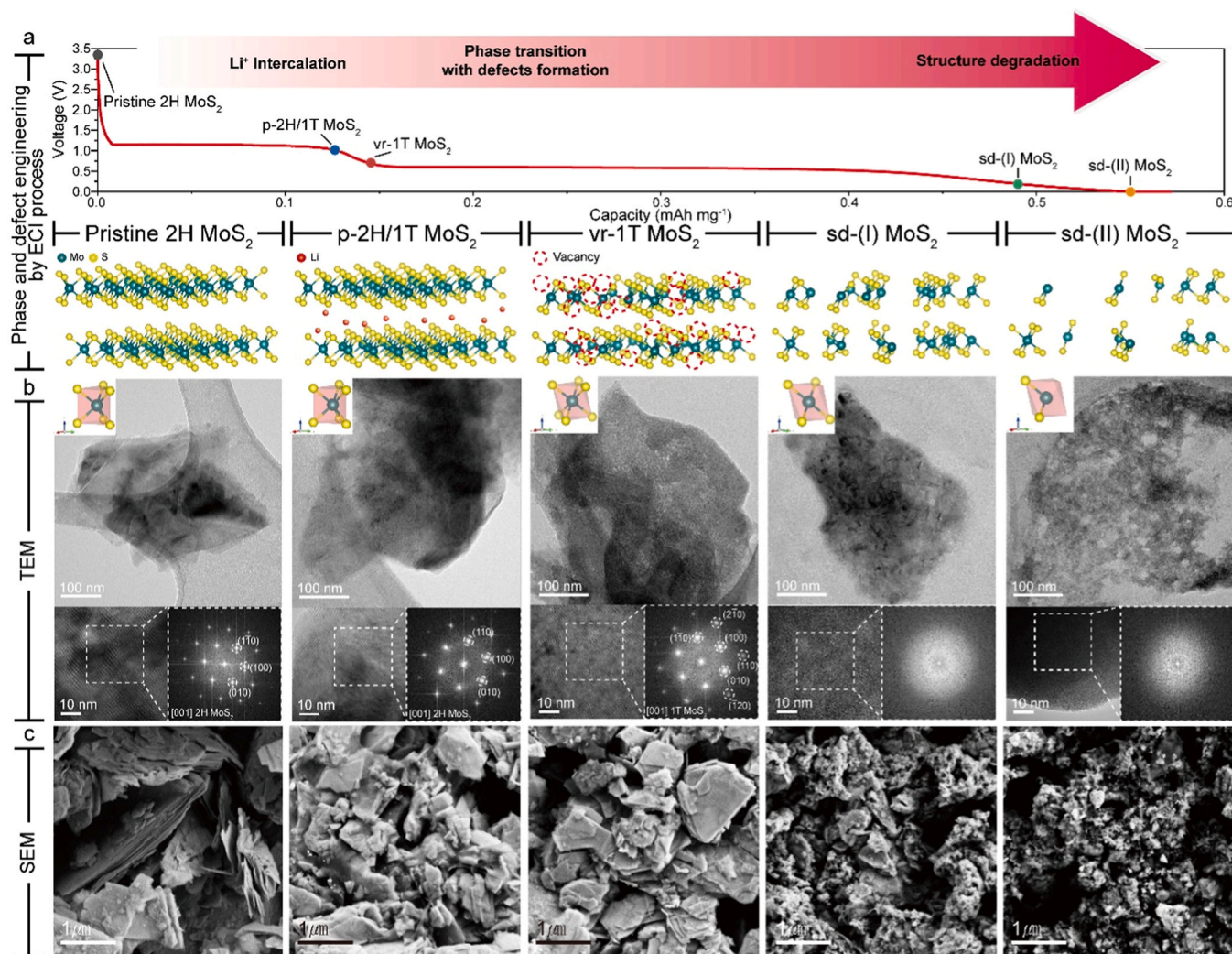
Subsequently, we confirmed that further ECI process led to the phase degradation of 1T MoS$_2$ into sub-nanoscale Mo around 0.6 V vs. Li/Li$^+$ (Eq. (2)) [60,61].

$$Li_xMoS_2 + (4-x)Li^+ + (4-x)e^- \rightarrow Mo + 2Li_2S \tag{2}$$

At the beginning of this reaction, the ECI process disturbed the local coordination environment of Mo and S in the MoS$_2$ structure, propagating the aforementioned vacancies to form voids. Therefore, the original 2H and 1T structural features of MoS$_2$ were destroyed (denoted as sd-(I) MoS$_2$). The application of further ECI up to 0 V vs. Li/Li$^+$ resulted in a phase transition in which the original layered morphology was completely lost and replaced by multiple pores (denoted as sd-(II) MoS$_2$). Furthermore, the FFT patterns did not exhibit sharp diffraction points, suggesting the presence of sub-nanoscale amorphous Mo particles (Fig. 1b). The pulverized particles in both sd-(I) MoS$_2$ and sd-(II) MoS$_2$ in the HRSEM images further support phase degradation originating from the deep ECI process (Fig. 1c).

3.2. Structural characterization of the ECI-processed MoS$_2$

The structural evolution of the MoS$_2$ catalysts during the ECI process was further characterized. XRD patterns of the MoS$_2$ samples were recorded at different ECI stages (Fig. 2a). Two broad diffraction peaks

Fig. 1. (a) Phase transition and surface defect formation of the MoS₂ catalysts by the ECI process and schematic of their structural evolution. (b) HRTEM images with selected area FFT, and (c) SEM images of pristine 2H MoS₂, p-2H/1T MoS₂, vr-1T MoS₂, sd-(I) MoS₂, and sd-(II) MoS₂.
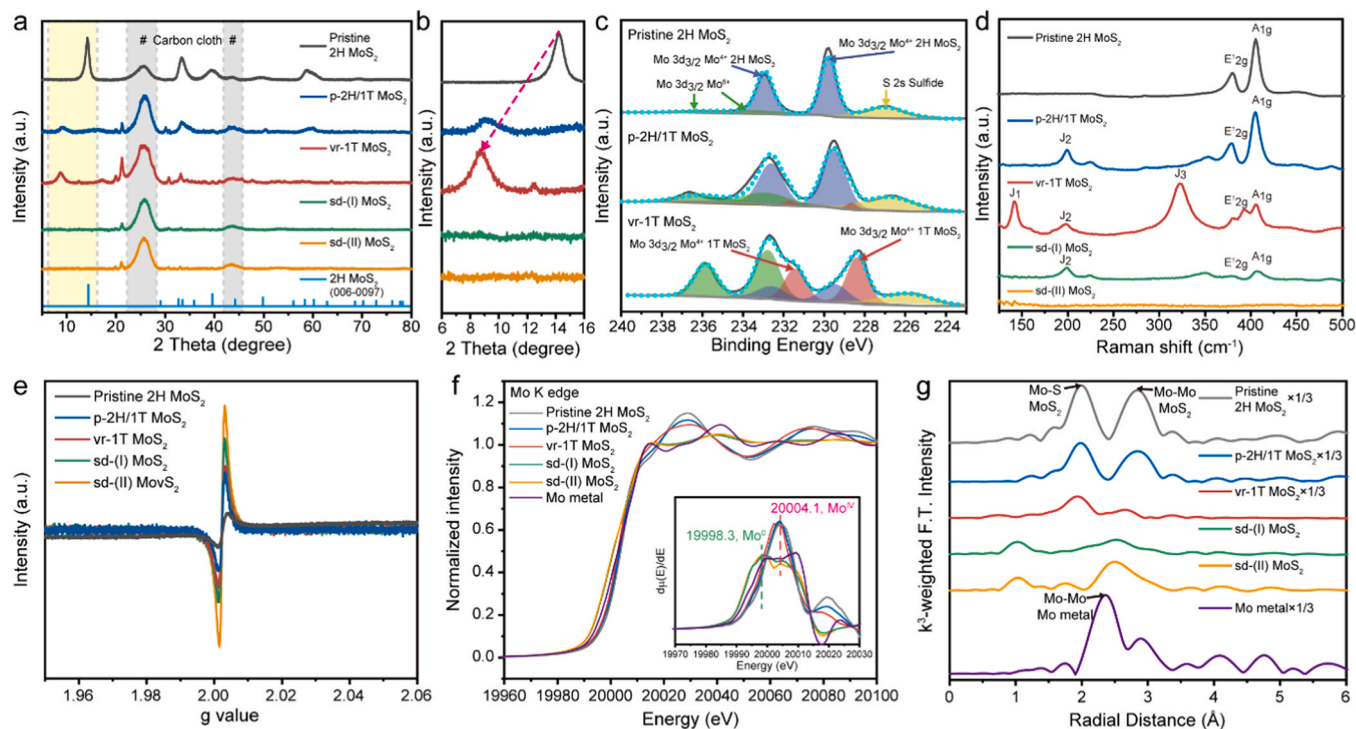
were observed at 2θ values of 25.7° and 43.5°, originating from the carbon cloth substrate in all the prepared samples [62,63]. The as-prepared 2H MoS₂ catalyst exhibited a sharp XRD peak at the 2θ value of 14.4°, corresponding to the characteristic (002) peak of the 2H MoS₂ phase (JCPDS reference code 006–0097).

The progressive ECI process modified the layered features of the MoS₂ catalyst. The magnified XRD patterns in the 2θ range of 6°–16° (Fig. 2b) showed that the (002) peak shifted toward lower 2θ values (14.4° (pristine 2H MoS₂) → 9.2° (p-2H/1T MoS₂) → 8.9° (vr-1T MoS₂)) [63–66], which resulted from the gradual intercalation of Li ions into the interlayer galleries and the resultant expansion of the (002) interlayer spacing along the c-axis. The significant shift in the (002) peak with its appreciable broadening indicated the phase transition of MoS₂ from the 2H to 1T phases [67–69] with the formation of surface vacancies. In contrast, sd-(I) MoS₂ and sd-(II) MoS₂ displayed no distinguishable XRD patterns, indicating that the features of the original layered MoS₂ phase were completely lost, which aligned with the HRTEM results (Fig. 1b).

XPS analysis was performed to characterize the change in the electronic state of MoS₂ during the progressive ECI process (Fig. 2c). The doublet corresponding to the Mo $3d_{5/2}$ and Mo $3d_{3/2}$ at 229.8 and 232.9 eV for the pristine 2H MoS₂ diminished gradually with the progress of ECI, whereas the new doublet for the 1T MoS₂ was observed at 228.4 and 231.4 eV, indicating successful transformation of the semiconducting 2H phase to the metallic 1T phase [17,29,70–72]. The

increasing peaks at 232.8 and 235.8 eV resulted from V_{Mo} formation on 1T MoS₂ surfaces [36,73,74]. This result also indicates that Li-ion implantation into the [MoS₆] slab may affect the Mo–S bonding properties and thus help stabilize the otherwise unstable 1T MoS₂ framework [75], which aligns with the XANES results, and will be discussed in further studies. Furthermore, the Raman spectra clearly demonstrated the evolution of the electronic structure of 2H MoS₂, as demonstrated by our suggested ECI process (Fig. 2d). During the ECI process, the characteristic phonon modes of the 2H MoS₂ phase at 379 and 405 cm^{-1} (E_{2g}^1 and A_{1g}) [65,66,71,76] were gradually suppressed, whereas those of the 1T MoS₂ phase in p-2H/1T MoS₂ and vr-1T MoS₂ appeared at 142, 199, and 323 cm^{-1} corresponding to the J₁, J₂, and J₃ modes, respectively [65,66, 71,76]. Moreover, both the 2H phase (E_{2g}^1 and A_{1g}) and 1T phases (J₁, J₂, and J₃) gradually diminished in sd-(I) MoS₂ and sd-(II) MoS₂ after further ECI, suggesting that the original layered MoS₂ structure was completely destroyed.

ESR analyses were conducted to investigate the density of lone-pair electrons in the samples. As the ECI process proceeded, a pair of opposite peaks with an S-shaped signal at approximately 3500 G (g = 2.003) became pronounced, which was associated with the formation of S vacancies and the resultant unsaturated coordination of Mo [17,29]. The increase in the intensity of the ESR peak with the progression of the ECI process indicated that the concentration of S vacancies increased during the ECI process (Fig. 2e) [77,78], which is also consistent with ICP-OES

Fig. 2. Characterization of phase and surface defect evolution. (a) XRD patterns, (b) magnified XRD patterns at (002) region, (c) XPS spectra, (d) Raman spectra, (e) ESR spectra, (f) ex situ XANES spectra, and (g) EXAFS profiles of pristine 2H MoS_2, p-2H/1T MoS_2, vr-1T MoS_2, sd-(I) MoS_2 and sd-(II) MoS_2.

results (Table S1). The gradual reduction in the S content in the catalysts supports the gradual formation of the S vacancies in the MoS_2 framework as the ECI process proceeded.

Because the ECI process readily tuned the electronic structure of Mo, we focused on XANES analysis at the Mo K-edge for a series of MoS_2 samples (Fig. 2f). The edge energies of the samples were evaluated using the first derivative of the corresponding XANES spectra (inset of Fig. 2f). The XANES profiles exhibited slight shifts, which gradually broadened as the ECI process progressed from pristine 2H MoS_2 to p-2H/1T MoS_2 to vr-1T MoS_2. This result was attributed to the loss of long-range order owing to the formation of S vacancies, which was also supported by the weakening intensities of the XRD peaks beyond the 2θ values of 30°. However, as the ECI process proceeded further, an appreciable shift was induced toward lower energies in the XANES profiles upon reduction of the 1T MoS_2 phase to the metallic Mo phase. The weak oscillation of the XANES spectra for sd-(I) MoS_2 and sd-(II) MoS_2 compared with that of the Mo foil implied the presence of a nanoscale metallic Mo domain in the corresponding samples.
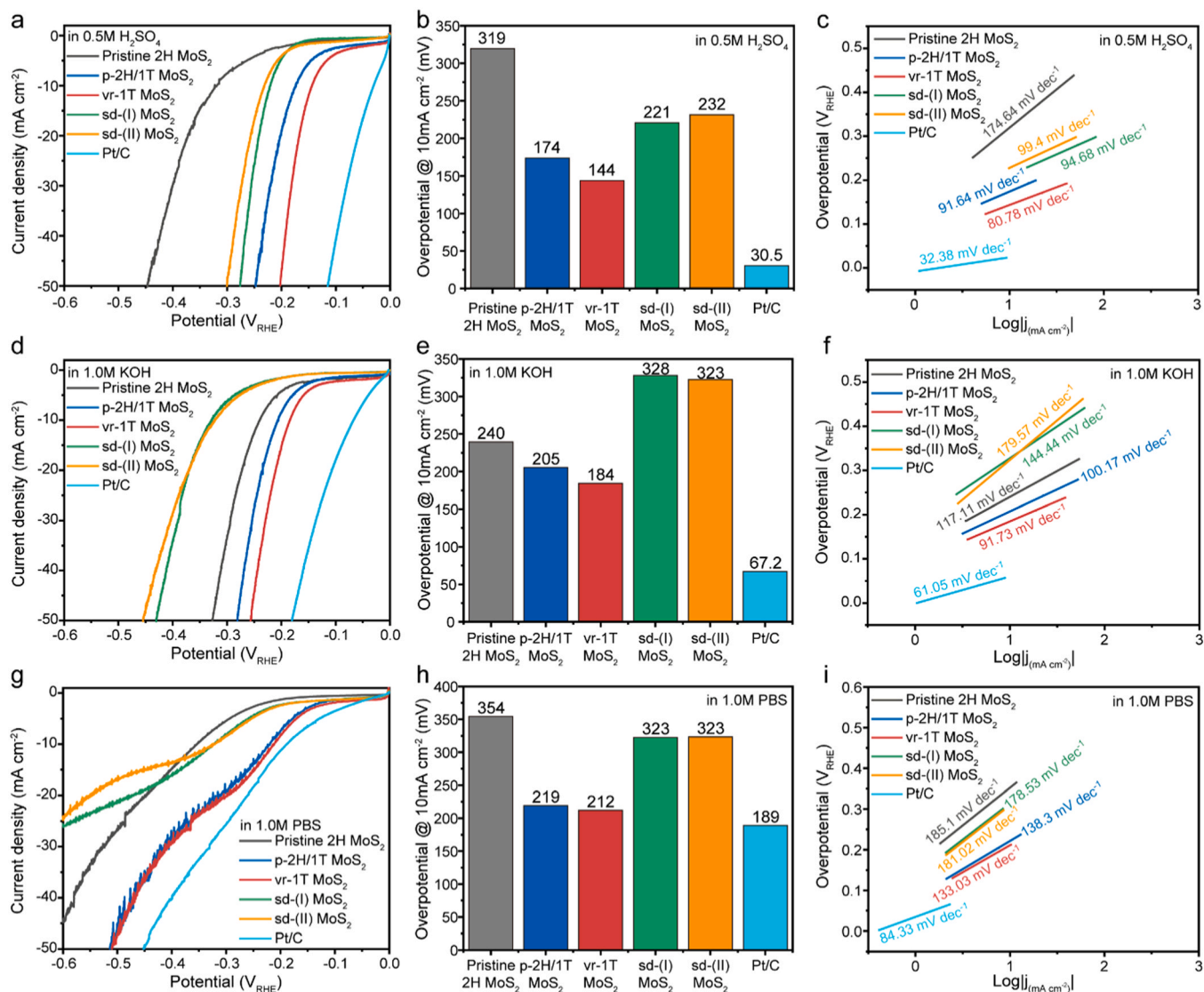
The EXAFS results were used to quantitatively investigate the interatomic bonding between Mo and neighboring Mo/S during the ECI process (Fig. 2g). The pristine 2H MoS_2 showed EXAFS peaks corresponding to the Mo–S and Mo–Mo paths at 2.0 and 2.9 Å, respectively. As the ECI process proceeded to p-2H/1T MoS_2 and vr-1T MoS_2, the EXAFS peaks corresponding to Mo–S and Mo–Mo decreased substantially, which was attributed to the formation of S vacancies [18,79]. The EXAFS fitting results (Figure S1) further confirmed that vr-1T MoS_2 exhibited a significantly lower coordination number for the Mo–S path (4.9 ± 0.6) than that of pristine 2H MoS_2 (5.5 ± 0.3). The increase in the degree of disorder (σ^2) also supported the presence of S vacancies ($0.0019 \pm 0.0006 \rightarrow 0.008 \pm 0.002$) in the MoS_2 framework. With more ECI processes, an additional small peak corresponding to the Mo–Mo path of the metallic Mo phase appeared at 2.4 Å for sd-(I) MoS_2 and sd-(II) MoS_2, suggesting that the basal plane surfaces with excess vacancies would be unstable, and thus the original MoS_2 framework was destroyed to transform into nanoscale metallic Mo [60]. The coordination numbers of the metallic Mo–Mo path for sd-(I) MoS_2 (5.3 ± 0.9) and

sd-(II) MoS_2 (9.9 ± 1.45) were significantly smaller than those of the reference Mo foil (14), indicating that the Mo nanodomains were formed by destroying the original MoS_2 framework (Eq. 2) at the deep ECI level [60,80]. The detailed fitting results are summarized in Tables S2–S8.

In order to verify the versatility of our ECI process to other transition metal dichalcogenides (TMD), we applied it to WS_2. As the degree of the ECI process increased (Figure S2), the sharp XRD peak at 14.3° corresponding to the (002) peak of the 2H WS_2 phase shifted to 14.1° (ECI(I)-WS_2) and 14.0° (ECI(II)-WS_2), indicating a successful phase transition from the 2H phase to the 1T phase. Moreover, the W 4*f* XPS doublet shifted toward lower binding energies (35.4/33.3 eV → 34.7/32.6 eV → 34.6/32.5 eV), which also demonstrated the same phase transition behavior [81–83]. Therefore, our ECI process can be readily applicable to other TMD catalysts.

3.3. HER performance evaluation of a series of MoS_2 catalysts over wide pH range

The obtained samples were evaluated as HER electrocatalysts in a three-electrode configuration, in which a graphite rod and hydrogen electrode served as the counter and reference electrodes, respectively. Further details are provided in the Experimental Section 2.5. To investigate the effects of phase transition and surface vacancies induced by the ECI process on the electrocatalytic performance of the MoS_2 catalysts, we evaluated their HER activities under acidic, alkaline, and pH-neutral conditions (Fig. 3). Fig. 3a–c show the polarization curves of the catalysts measured using linear scanning voltammetry at a scan rate of 5 mV s^{-1} in 0.5 M H_2SO_4 electrolytes, along with commercial carbon-supported 20 wt% Pt catalysts (Pt/C). A volcano-like dependence of HER performance is observed for the degree of ECI. As shown in Fig. 3b, the overpotential required to achieve an HER current of 10 mA cm^{-2} (denoted as η_{10}) decreases from pristine 2H MoS_2 (319 mV) to p-2H/1T MoS_2 (174 mV) to vr-1T MoS_2 (144 mV), and then increases from vr-1T MoS_2 to sd-(I) MoS_2 (221 mV) to sd-(II) MoS_2 (232 mV). In addition, the mass activities of catalysts (Figures S3a and S3b) were also calculated by using the mass loading of catalysts (Table S11). The η_{10} calculated from

Fig. 3. Electrochemical HER performance of a series of catalysts in different electrolytes. (a) HER polarization curves measured at a scan rate of 5 mV s^{-1}, (b) overpotentials at the current density of 10 mA cm^{-2} (η_{10}), and (c) Tafel plots of the catalysts in a 0.5 M H$_2$SO$_4$ electrolyte. HER polarization curves with same conditions in (d–f) 1 M KOH and (g–i) 1 M PBS electrolytes.

mass activity profiles decreased from pristine 2H MoS$_2$ (410 mV) to p-2H/1T MoS$_2$ (207 mV) to vr-1T MoS$_2$ (169 mV), and then increases from vr-1T MoS$_2$ to sd-(I) MoS$_2$ (228 mV) to sd-(II) MoS$_2$ (235 mV). Such volcanic HER activity suggests the presence of an optimal level of ECI for tuning the structural and electronic properties of MoS$_2$ catalysts. The calculated Tafel slopes of the catalysts also exhibit a similar volcano-like trend (Fig. 3c), as observed in the η_{10} values. All the catalysts show Tafel slopes ranging from 80–175 mV dec^{-1} (175, 92, 81, 95, and 99 mV dec^{-1} for pristine 2H MoS$_2$, p-2H/1T MoS$_2$, vr-1T MoS$_2$, sd-(I) MoS$_2$, and sd-(II) MoS$_2$, respectively), indicating the Volmer–Heyrovsky reaction pathway with the H adsorption reaction (Volmer step, * + H$^+$ + e$^-$ → *H) as the rate-determining step [84,85]. Among the catalysts, the lowest Tafel slope (81 mV dec^{-1}) and the charge transfer resistance value (0.97 Ω cm^{-2}, Figure S4a) indicated that vr-1T MoS$_2$ was effective at facilitating the Volmer reaction owing to its defective but metallic conducting nature. This result was also supported by the highest ECSA values among all the electrolytes used in this study (Figures S5–S7; 1534, 1944.75, and 846.5 cm^2 in 0.5 M H$_2$SO$_4$, 1.0 M KOH, and 1.0 M PBS, respectively), which were 2.4–12.7 times higher than that for the pristine 2H MoS$_2$ catalyst. Table S9 lists the HER performance values of the MoS$_2$ catalysts in this study in comparison with previously reported
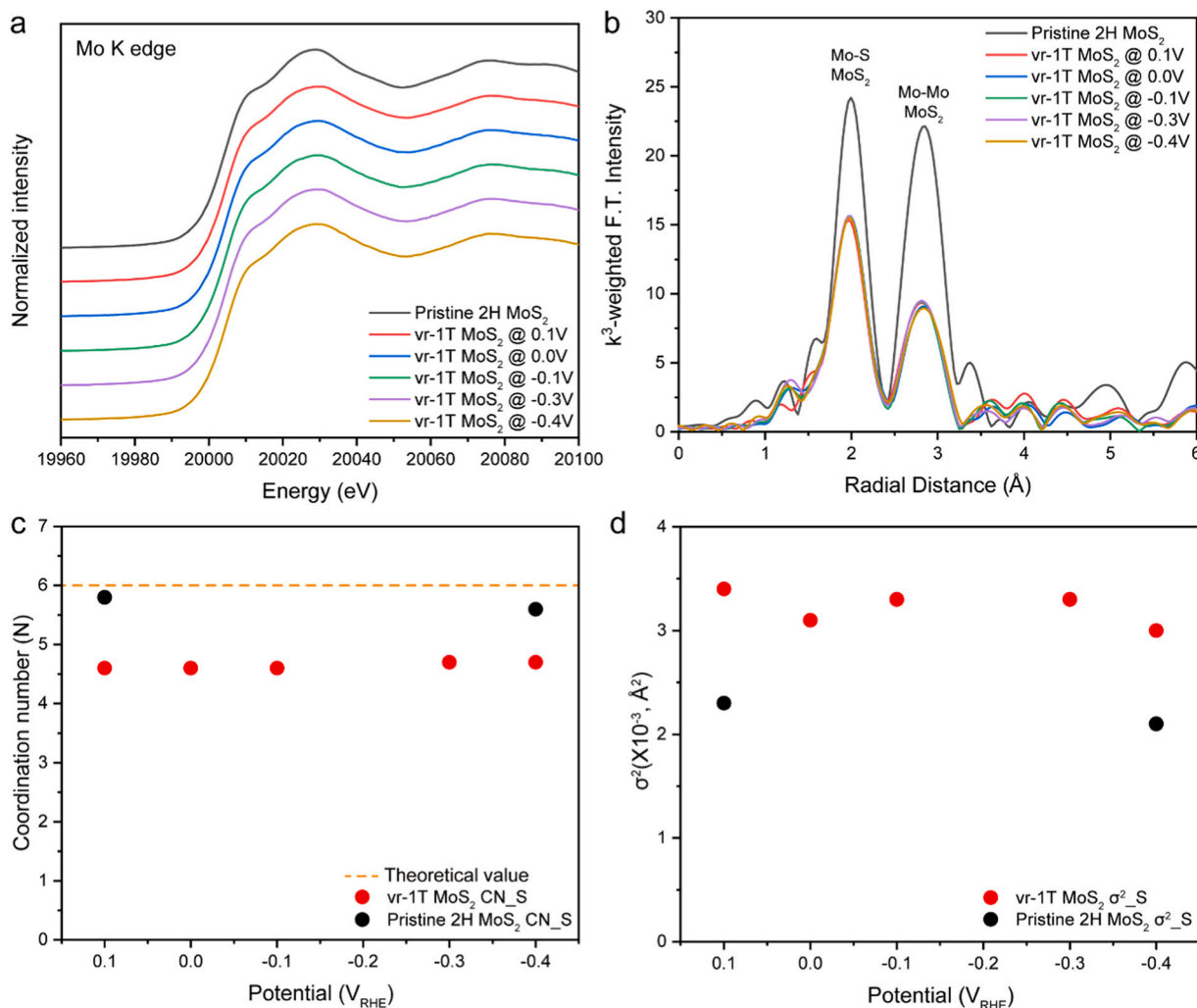
modified MoS$_2$-based HER catalysts, highlighting the excellent HER performance of vr-1T MoS$_2$ compared with other MoS$_2$-based catalysts with simple phases, defects, and electronic structural modifications. Furthermore, vr-1T MoS$_2$ maintained its original HER activity during long-term operation. After 1000 cycles of CV cycles, a negligible change was observed in the LSV profiles (Figure S8a). Stability tests performed using CP at a current density of 10 mA cm^{-2} showed a negligible activity loss in 0.5 M H$_2$SO$_4$ electrolyte even after 100 h (Figure S8b). Moreover, the TEM images (Figure S9) and ICP-OES results (Table S1) of the vr-1T MoS$_2$ before and after long-term HER operation confirmed that the elemental composition and structural properties remained unchanged, which is also associated with the good stability of MoS$_2$ surfaces within the potentials for HER in acid media [86].

The vr-1T MoS$_2$ catalyst maintained its superior HER performance in 1.0 M KOH (Figs. 3d–3f) and 1 M PBS (Figs. 3g–3i) solutions. In 1.0 M KOH, volcano-like η_{10} profiles were observed with the η_{10} value of vr-1T MoS$_2$ (184 mV) lower than those of pristine 2H MoS$_2$ (240 mV), p-2H/1T MoS$_2$ (205 mV), sd-(I) MoS$_2$ (328 mV), and sd-(II) MoS$_2$ (323 mV). The same tendency was maintained even under the mass activity considerations (Figures S3c and S3d). Moreover, the calculated Tafel slope values in 1.0 M KOH showed a similar volcano-like trend in the acidic

electrolyte. The vr-1T MoS$_2$ achieved the lowest Tafel slope (92 mV dec^{-1}), which was attributed to the favorable Volmer step on the vr-1T MoS$_2$ surface, even under alkaline conditions. The lowest charge transfer resistance (2.27 Ω cm^{-2}) of vr-1T MoS$_2$ also supported the facile Volmer step in the HER process (Figure S4b). Both the sd-(I) MoS$_2$ and sd-(II) MoS$_2$ catalysts exhibited relatively larger η_{10} values, which might be attributed to the strong H binding on the Mo surfaces formed by the deep ECI process [87]. Although in 1.0 M PBS, the overall trends in η_{10} values, Tafel slopes, and catalytic life span remained similar, the HER performance deteriorated. Such deteriorated HER performance in 1.0 M PBS solution was often observed in previous studies using PBS-based electrolytes [88–93]; this was attributed to the sluggish mass transport rate over a prolonged cycle. However, the vr-1T MoS$_2$ showed decent η_{10} value and Tafel slope of 212 mV and 133 mV dec^{-1} compared with other counterparts of pristine 2H MoS$_2$ (354 mV and 185 mV dec^{-1}), p-2H/1T MoS$_2$ (219 mV and 138 mV dec^{-1}), sd-(I) MoS$_2$ (323 mV and 181 mV dec^{-1}), and sd-(II) MoS$_2$ (323 mV and 138 mV dec^{-1}) in 1.0 M PBS electrolyte. In the mass activity consideration, similar tendency was maintained, further supporting the high electrochemical activity of vr-1T MoS$_2$. Unlike the robust performance in 0.5 M H$_2$SO$_4$ electrolyte, when tested in 1.0 M KOH and 1.0 M PBS electrolytes, the vr-1T MoS$_2$ catalyst exhibited an initial drop in their activity for the initial 10 h and a plateau for remaining duration. The main reason for the initial activity

loss can be attributed to the partial dissolution of S^{2-} ions alkaline and neutral electrolytes. However, because the catalyst surface are readily passivated by Mo-containing hydroxide layers, the activity would not further decay [94]. The pH-universal HER performance of the optimized vr-1T MoS$_2$ catalyst was compared with those of other state-of-the-art modified MoS$_2$-based catalysts (Figure S10 and Table S10). In mass-specific assessments, our optimized vr-1T MoS$_2$ catalyst exhibited outstanding HER performance (*i.e.*, mA mg$_{MoS2}^{-1}$ and η_{10}) compared to other MoS$_2$-based catalysts (Figure S3 and Table S12). The vr-1T MoS$_2$ catalyst not only exhibited pH-universal HER performance through the facile modification of the catalytic active phase and simultaneous incorporation of defects over the MoS$_2$ framework, but also demonstrated outstanding HER performance over a wide pH range compared with complex heterostructures that engage in single-atom decoration and biphasic composites.

We also performed a similar ECI process using Na ions instead of Li ions (Figure S11). Two distinct cathodic peaks around 0.8 and 0.0 V versus the standard reduction potential of Na (V$_{Na}$) in the CV curve indicated that Na ion implantation also led to the phase transition of the 2H MoS$_2$ phase to the 1T MoS$_2$ phase, similar in the process using Li ions (Fig. 2). The HER performance of the ECI-processed MoS$_2$ catalysts by Na ions taken at different potentials (namely, Na-ECI(I)-MoS$_2$ and Na-ECI(II)-MoS$_2$ as denoted in Figure S11a) was compared. Na-ECI(I)-MoS$_2$

Fig. 4. In situ XAFS analyses of vr-1T MoS$_2$ measured at Mo K-edge in a 0.5 M H$_2$SO$_4$ electrolyte. (a) In situ XANES profiles from 0.1 V$_{RHE}$ (top) to –0.4 V$_{RHE}$ (bottom) and (b) corresponding EXAFS profiles along with those of pristine 2H MoS$_2$ as reference spectra. (c) EXAFS-fitted coordination numbers of Mo–S (CN_S) path for vr-1T MoS$_2$ (red) and pristine 2H MoS$_2$ (black) catalysts as a function of applied potentials. (d) Debye–Waller factors of the Mo–S (σ^2_S) path for vr-1T MoS$_2$ (red) and pristine 2H MoS$_2$ (black) catalysts.

exhibited superior HER performance with its η_{10} value being 129 mV, suggesting that Na ions also can be utilized as an effective carrier ion in the ECI process.

3.4. In situ XAFS analyses at the Mo K-edge

We performed in situ XAFS at electrochemical potentials for HER in the range of 0.1 V_{RHE} to –0.4 V_{RHE} (Fig. 4) in 0.5 M H_2SO_4 solution to further analyze the physicochemical properties of vr-1T MoS_2 during HER. For comparison, pristine 2H MoS_2 catalyst was characterized using in situ XAFS measurement at 0.1 V_{RHE} and –0.4 V_{RHE} (Figure S12) (See the Experimental Section 2.6 for further details). No significant change was observed in the XANES profiles of the vr-1T MoS_2 and pristine 2H MoS_2 catalysts over the entire potential range (Fig. 4a), indicating that neither catalyst underwent structural degradation during the HER process. The negligible changes in the Mo–S and Mo–Mo peaks in the EXAFS profiles of vr-1T MoS_2 also supported the fact that the structural and electronic properties induced by the ECI process remained robust during the HER, and the surface vacancies persistently served as catalytically active sites for the HER (Fig. 4b).

EXAFS fitting was performed to further investigate the local structural environment around Mo with a focus on the coordination number (CN) and Debye–Waller factor (σ^2) values of the Mo–S and Mo–Mo paths (Figures S13–S14 and Tables S13–S14). Compared with pristine 2H MoS_2 catalyst, the CN values for the Mo–S (CN_S) path of vr-1T MoS_2 catalyst appreciably decreased (5.8 ± 0.4 for pristine 2H MoS_2 → 4.6 ± 0.4 for vr-1T MoS_2). The decrease in the CN_S value, a key indicator of S vacancies in vr-1T MoS_2, remained almost unchanged throughout the potential range for in situ measurements (Fig. 4c), indicating a robust structural 1T MoS_2 framework while maintaining S vacancies. In particular, our in situ EXAFS fitting results demonstrated the critical role of S vacancies in facilitating H adsorption (Volmer step) during the HER process. As the potential increased negatively (Fig. 4d), the σ^2 values for the Mo–S path (σ^2_S) decreased. At 0.1 V_{RHE}, where H adsorption is thermodynamically unfavorable, vr-1T MoS_2 exhibited a σ^2_S value of 3.4 ± 1.0. However, at –0.4 V_{RHE}, the σ^2_S value decreased to 3 ± 0.1, which was due to the H adsorption on the catalytic active site, thereby reducing the degree of disorder for the Mo–S path. The pristine 2H MoS_2 catalyst exhibited a similar trend of reduction in the σ^2_S value (2.3 ± 0.7 at 0.1 V_{RHE} → 2.1 ± 0.7 at –0.4 V_{RHE}), further supporting the involvement of a catalytic active site in the Mo–S bonding. In fact, such a decrease in Debye-Waller factor upon H adsorption has been widely observed in the Pt-based catalysts [95–97], where the strong chemisorption of H and Pt atoms limits the motion of Pt atoms [97]. Likewise, the degree of disordering for the Mo–S path could likely be reduced by H adsorption. Based on the σ^2_S value, the enhanced HER activity of vr-1T MoS_2 was attributed to the optimal binding mode of *H intermediates on the populated catalytic active sites (S vacancies) and the enhanced charge transfer rate by the modified electronic structure (semiconducting → metallic) enabled by the ECI process.

3.5. DFT calculations

DFT calculations were carried out to identify the respective effects of phase transition and vacancy defects generation in improving HER performance. Firstly, the formation energies of 2H and 1T family (*i.e.*, 1T, 1T`, 1T``, and 1T```) of MoS_2 structure (Figure S15) were calculated and compared. The calculated values of formation energy per atom for 2H, 1T, 1T`, 1T``, and 1T``` MoS_2 structures are found to be –0.777 eV, –0.496 eV, –0.589 eV, –0.557 eV, and –0.588 eV, respectively, indicating that 1T`, 1T``, and 1T``` MoS_2 structures are the more favorable derivative in 1T family of MoS_2, consistent with the literature [51,54]. The previous experimental results also noted that the 1T MoS_2 structural motif are readily distorted to form its derivatives [52,75]. A comparison of our DFT obtained formation energies, lattice constants, and vacancy formation energies with previous DFT results is presented in Table S15.

Overall the results are consistent with the previous DFT reports [53,98]. In addition, the results of the DFT calculations of vacancy formation energies show that, in general, the formation of S-vacancy is thermodynamically more favorable compared to the formation of Mo vacancies (Table S15). Therefore, the below HER-related discussion is mostly limited to the MoS_2 structures with and without S vacancies. To this end, we constructed MoS_2 model surfaces to represent pristine 2H MoS_2 (2H MoS_2), vr-1T MoS_2 (1T` $MoS_2$, *Sv*-1T` MoS_2, 1T`` $MoS_2$, and *Sv*-1T`` MoS_2, where *Sv* is referred to as a S-vacancy) catalysts investigated in this work.

The binding energy of hydrogen (Table S16), a key HER intermediate in acid electrolytes, is calculated on all possible surface sites (Figure S16). The DFT calculated binding energy of hydrogen is then used to construct the HER free energy diagrams shown in Figs. 5a and S17. It was observed that the ΔG(*H) value was significantly lowered on 1T` MoS_2 (0.15 eV) and 1T`` $MoS_2$ (0.40 eV) than 2H $MoS_2$ (1.77 eV), indicating first that the structural modification was effective in facilitating the HER process. In addition, *H adsorption became almost thermoneutral on the S-vacancies on 1T` $MoS_2$ (*Sv*-1T` $MoS_2$, –0.22 eV) and 1T`` MoS_2 (*Sv*-1T`` MoS_2, –0.12 eV), supporting the facile Volmer step and the resultant high HER activity of vr-1T MoS_2 catalyst in the experimental results (Fig. 3a). We also found that the S vacancy on 2H MoS_2 (*Sv*-2H MoS_2) can facilitate the HER process with its nearly thermoneutral binding energy of –0.05 eV (Figure S17). However, the S vacancy is unlikely on 2H MoS_2 because of the relatively high S vacancy formation energy (0.037 eV) compared with those on 1T MoS_2 (–0.051 eV) and 1T`` MoS_2 (0.018 eV). Therefore, we could rule out the *Sv*-2H MoS_2 from further considerations because it is rarely feasible from the experimental viewpoints.
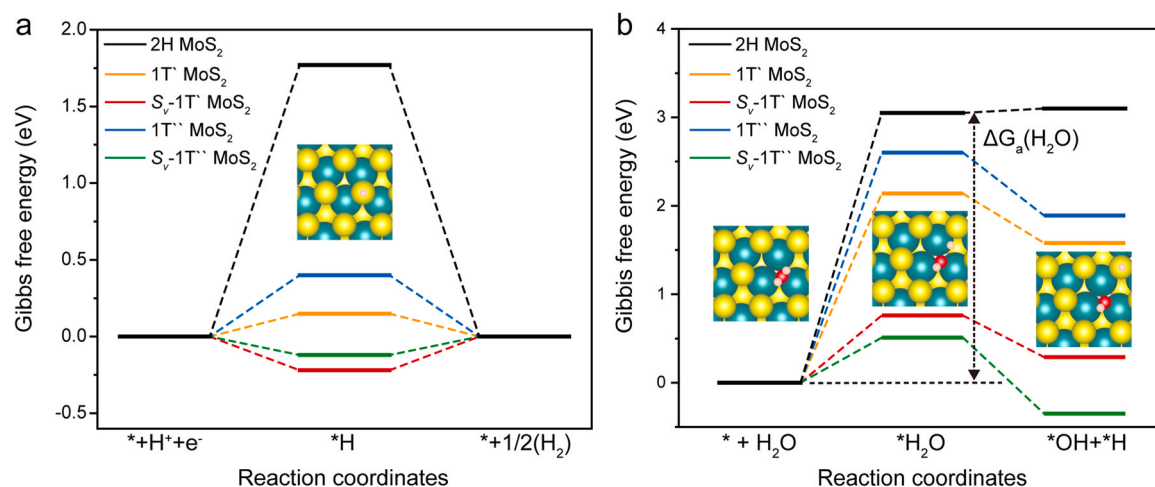
We also constructed the free energy diagrams (Fig. 5b) involving the energy barrier for water dissociation (ΔG_a(H_2O)) because the HER process in alkaline and neutral electrolytes are mainly controlled by the water dissociation reaction on the catalyst surfaces. It is observed that the S vacancy assisted water dissociation reaction is more favorable (*e.g.*, 0.75 eV on *Sv*-1T` MoS_2 and 0.51 eV on *Sv*-1T`` $MoS_2$) than the water dissociation reaction on other $MoS_2$ surfaces without S vacancies (*e.g.*, 2.14 eV on 1T` $MoS_2$, 2.6 eV on 1T`` MoS_2, and 3.05 eV on 2H MoS_2), supporting again the enhanced HER activity and kinetics of vr-1T MoS_2 compared with those of 2H pristine MoS_2 (Figs. 3d and 3g).

4. Conclusions

We demonstrated an ECI process for improving electrocatalytic performance by tuning the structural and electronic properties of a given catalyst. Our ECI process successfully modified the MoS_2 catalyst as a model catalyst to exhibit high HER activity, low overpotential (η_{10}, 144 mV), and long-term stability with negligible activity loss up to 100 h. Our combined HR-TEM, Raman, and in situ XAFS analyses revealed that the enhanced HER capability of the ECI-processed MoS_2 catalyst was attributed to the modified electronic properties and populated catalytic active sites on the basal planes of the MoS_2 catalyst, resulting in a more favorable Volmer step compared with the pristine MoS_2 catalyst. Specifically, progressive Li-ion implantation induced a phase transition from the semiconducting 2H phase to the metallic 1T phase concurrently with vacancy formation, which facilitated the HER process. Therefore, our study highlights the potential of the ECI process as a universal approach for converting nonactive catalytic sites into active sites.

CRediT authorship contribution statement

Hyung Mo Jeong: Conceptualization, Funding acquisition, Project administration, Resources, Supervision, Writing – original draft, Writing – review & editing. **Ji Hoon Lee:** Writing – review & editing, Writing – original draft, Supervision, Investigation, Funding acquisition. **Bipin Lamichhane:** Formal analysis, Investigation, Methodology, Writing –

Fig. 5. DFT calculated (a) HER free energy diagram in acidic electrolytes and (b) barrier for water dissociation on a series of MoS_2 surfaces. The inset figures are top view of the 1T`` MoS_2 slab with corresponding reaction intermediates. Mo: turquoise, S: yellow, O: red, and H: pink.

Appendix A. Supporting information

Supplementary data associated with this article can be found in the online version at doi:10.1016/j.apcatb.2024.124037.

References

[1] T.R. Karl, K.E. Trenberth, Modern global climate change, Science 302 (2003) 1719–1723.
[2] B. Obama, The irreversible momentum of clean energy, Science 355 (2017) 126–129.
[3] K. Sumida, D.L. Rogow, J.A. Mason, T.M. McDonald, E.D. Bloch, Z.R. Herm, T.-H. Bae, J.R. Long, Carbon dioxide capture in metal–organic frameworks, Chem. Rev. 112 (2012) 724–781.
[4] D.M. D'Alessandro, B. Smit, J.R. Long, Carbon dioxide capture: prospects for new materials, Angew. Chem. Int. Ed. 49 (2010) 6058–6082.
[5] B.M. Tackett, E. Gomez, J.G. Chen, Net reduction of CO2 via its thermocatalytic and electrocatalytic transformation reactions in standard and hybrid processes, Nat. Catal. 2 (2019) 381–386.
[6] J. Zhu, L. Hu, P. Zhao, L.Y.S. Lee, K.-Y. Wong, Recent advances in electrocatalytic hydrogen evolution using nanoparticles, Chem. Rev. 120 (2020) 851–918.
[7] J.D. Benck, T.R. Hellstern, J. Kibsgaard, P. Chakthranont, T.F. Jaramillo, Catalyzing the hydrogen evolution reaction (HER) with molybdenum sulfide nanomaterials, ACS Catal. 4 (2014) 3957–3971.
[8] S.J. Davis, N.S. Lewis, M. Shaner, S. Aggarwal, D. Arent, I.L. Azevedo, S.M. Benson, T. Bradley, J. Brouwer, Y.-M. Chiang, C.T.M. Clack, A. Cohen, S. Doig, J. Edmonds, P. Fennell, C.B. Field, B. Hannegan, B.-M. Hodge, M.I. Hoffert, E. Ingersoll, P. Jaramillo, K.S. Lackner, K.J. Mach, M. Mastrandrea, J. Ogden, P.F. Peterson, D. L. Sanchez, D. Sperling, J. Stagner, J.E. Trancik, C.-J. Yang, K. Caldeira, Net-zero emissions energy systems, Science 360 (2018) eaas9793.
[9] Y. Jiao, Y. Zheng, M. Jaroniec, S.Z. Qiao, Design of electrocatalysts for oxygen- and hydrogen-involving energy conversion reactions, Chem. Soc. Rev. 44 (2015) 2060–2086.
[10] J.A. Turner, Sustainable hydrogen production, Science 305 (2004) 972–974.
[11] W.-F. Chen, J.T. Muckerman, E. Fujita, Recent developments in transition metal carbides and nitrides as hydrogen evolution electrocatalysts, Chem. Commun. 49 (2013) 8896–8909.
[12] Y. Shi, B. Zhang, Recent advances in transition metal phosphide nanomaterials: synthesis and applications in hydrogen evolution reaction, Chem. Soc. Rev. 45 (2016) 1529–1541.
[13] Y. Guo, T. Park, J.W. Yi, J. Henzie, J. Kim, Z. Wang, B. Jiang, Y. Bando, Y. Sugahara, J. Tang, Y. Yamauchi, Nanoarchitectonics for transition-metal-sulfide-based electrocatalysts for water splitting, Adv. Mater. 31 (2019) 1807134.
[14] H. Li, X. Jia, Q. Zhang, X. Wang, Metallic transition-metal dichalcogenide nanocatalysts for energy conversion, Chem 4 (2018) 1510–1537.
[15] X. Chia, A.Y.S. Eng, A. Ambrosi, S.M. Tan, M. Pumera, Electrochemistry of nanostructured layered transition-metal dichalcogenides, Chem. Rev. 115 (2015) 11941–11966.
[16] L. Lei, D. Huang, G. Zeng, M. Cheng, D. Jiang, C. Zhou, S. Chen, W. Wang, A fantastic two-dimensional MoS2 material based on the inert basal planes activation: electronic structure, synthesis strategies, catalytic active sites, catalytic and electronics properties, Coord. Chem. Rev. 399 (2019) 213020.
[17] Y. Yin, J. Han, Y. Zhang, X. Zhang, P. Xu, Q. Yuan, L. Samad, X. Wang, Y. Wang, Z. Zhang, P. Zhang, X. Cao, B. Song, S. Jin, Contributions of phase, sulfur vacancies, and edges to the hydrogen evolution reaction catalytic activity of porous molybdenum disulfide nanosheets, J. Am. Chem. Soc. 138 (2016) 7965–7972.
[18] Y. Huang, Y. Sun, X. Zheng, T. Aoki, B. Pattengale, J. Huang, X. He, W. Bian, S. Younan, N. Williams, J. Hu, J. Ge, N. Pu, X. Yan, X. Pan, L. Zhang, Y. Wei, J. Gu, Atomically engineering activation sites onto metallic 1T-MoS2 catalysts for enhanced electrochemical hydrogen evolution, Nat. Commun. 10 (2019) 982.
[19] D. Voiry, M. Salehi, R. Silva, T. Fujita, M. Chen, T. Asefa, V.B. Shenoy, G. Eda, M. Chhowalla, Conducting MoS2 nanosheets as catalysts for hydrogen evolution reaction, Nano Lett. 13 (2013) 6222–6227.
[20] Y. Yu, G.-H. Nam, Q. He, X.-J. Wu, K. Zhang, Z. Yang, J. Chen, Q. Ma, M. Zhao, Z. Liu, F.-R. Ran, X. Wang, H. Li, X. Huang, B. Li, Q. Xiong, Q. Zhang, Z. Liu, L. Gu, Y. Du, W. Huang, H. Zhang, High phase-purity 1T′-MoS2- and 1T′-MoSe2-layered crystals, Nat. Chem. 10 (2018) 638–643.
[21] S. Bolar, S. Shit, J.S. Kumar, N.C. Murmu, R.S. Ganesh, H. Inokawa, T. Kuila, Optimization of active surface area of flower like MoS2 using V-doping towards

enhanced hydrogen evolution reaction in acidic and basic medium, Appl. Catal. B Environ. 254 (2019) 432–442.

[22] Z. Luo, Y. Ouyang, H. Zhang, M. Xiao, J. Ge, Z. Jiang, J. Wang, D. Tang, X. Cao, C. Liu, W. Xing, Chemically activating MoS2 via spontaneous atomic palladium interfacial doping towards efficient hydrogen evolution, Nat. Commun. 9 (2018) 2120.

[23] T. Dong, X. Zhang, P. Wang, H.-S. Chen, P. Yang, Formation of Ni-doped MoS2 nanosheets on N-doped carbon nanotubes towards superior hydrogen evolution, Electrochim. Acta 338 (2020) 135885.

[24] J. Wang, W. Fang, Y. Hu, Y. Zhang, J. Dang, Y. Wu, B. Chen, H. Zhao, Z. Li, Single atom Ru doping 2H-MoS2 as highly efficient hydrogen evolution reaction electrocatalyst in a wide pH range, Appl. Catal. B Environ. 298 (2021) 120490.

[25] Y. Shi, Y. Zhou, D.-R. Yang, W.-X. Xu, C. Wang, F.-B. Wang, J.-J. Xu, X.-H. Xia, H.-Y. Chen, Energy level engineering of MoS2 bY Transition-metal Doping for Accelerating Hydrogen Evolution Reaction, J. Am. Chem. Soc. 139 (2017) 15479–15485.

[26] S. Deng, M. Luo, C. Ai, Y. Zhang, B. Liu, L. Huang, Z. Jiang, Q. Zhang, L. Gu, S. Lin, X. Wang, L. Yu, J. Wen, J. Wang, G. Pan, X. Xia, J. Tu, Synergistic doping and intercalation: realizing deep phase modulation on mos2 arrays for high-efficiency hydrogen evolution reaction, Angew. Chem. Int. Ed. 58 (2019) 16289–16296.

[27] A.D. Nguyen, T.K. Nguyen, C.T. Le, S. Kim, F. Ullah, Y. Lee, S. Lee, K. Kim, D. Lee, S. Park, J.-S. Bae, J.I. Jang, Y.S. Kim, Nitrogen-plasma-treated continuous monolayer MoS2 for improving hydrogen evolution reaction, ACS Omega 4 (2019) 21509–21515.

[28] G. Ye, Y. Gong, J. Lin, B. Li, Y. He, S.T. Pantelides, W. Zhou, R. Vajtai, P.M. Ajayan, Defects engineered monolayer MoS2 for improved hydrogen evolution reaction, Nano Lett. 16 (2016) 1097–1103.

[29] X. Wang, Y. Zhang, H. Si, Q. Zhang, J. Wu, L. Gao, X. Wei, Y. Sun, Q. Liao, Z. Zhang, K. Ammarah, L. Gu, Z. Kang, Y. Zhang, Single-atom vacancy defect to trigger high-efficiency hydrogen evolution of MoS2, J. Am. Chem. Soc. 142 (2020) 4298–4308.

[30] T. Ali, W. Qiao, D. Zhang, W. Liu, S. Sajjad, C. Yan, R. Su, Surface sulfur vacancy engineering of metal sulfides promoted desorption of hydrogen atoms for enhanced electrocatalytic hydrogen evolution, J. Phys. Chem. C 125 (2021) 12707–12712.

[31] H. Sun, X. Xu, H. Kim, W. Jung, W. Zhou, Z. Shao, Electrochemical water splitting: bridging the gaps between fundamental research and industrial applications, ENERGY Environ. Mater. 6 (2023) e12441.

[32] Z.-Y. Yu, Y. Duan, X.-Y. Feng, X. Yu, M.-R. Gao, S.-H. Yu, Clean and affordable hydrogen fuel from alkaline water splitting: past, recent progress, and future prospects, Adv. Mater. 33 (2021) 2007100.

[33] H. Li, C. Tsai, A.L. Koh, L. Cai, A.W. Contryman, A.H. Fragapane, J. Zhao, H.S. Han, H.C. Manoharan, F. Abild-Pedersen, J.K. Nørskov, X. Zheng, Activating and optimizing MoS2 basal planes for hydrogen production through the formation of strained sulphur vacancies, Nat. Mater. 15 (2016) 48–53.

[34] Y. Kim, D.H.K. Jackson, D. Lee, M. Choi, T.-W. Kim, S.-Y. Jeong, H.-J. Chae, H.W. Kim, N. Park, H. Chang, T.F. Kuech, H.J. Kim, Situ electrochemical activation of atomic layer deposition coated MoS2 basal planes for efficient hydrogen evolution reaction, Adv. Funct. Mater. 27 (2017) 1701825.

[35] L. Li, Z. Qin, L. Ries, S. Hong, T. Michel, J. Yang, C. Salameh, M. Bechelany, P. Miele, D. Kaplan, M. Chhowalla, D. Voiry, Role of sulfur vacancies and undercoordinated Mo regions in MoS2 nanosheets toward the evolution of hydrogen, ACS Nano 13 (2019) 6824–6834.

[36] S.-S. Chee, W.-J. Lee, Y.-R. Jo, M.K. Cho, D. Chun, H. Baik, B.-J. Kim, M.-H. Yoon, K. Lee, M.-H. Ham, Atomic vacancy control and elemental substitution in a monolayer molybdenum disulfide for high performance optoelectronic device arrays, Adv. Funct. Mater. 30 (2020) 1908147.

[37] X. Wang, J. Wu, Y. Zhang, Y. Sun, K. Ma, Y. Xie, W. Zheng, Z. Tian, Z. Kang, Y. Zhang, Vacancy defects in 2D transition metal dichalcogenide electrocatalysts: from aggregated to atomic configuration, Adv. Mater. 35 (2023) 2206576.

[38] X. Wang, Z. Zhang, J. Wu, Z. Zhang, Q. Liao, Z. Kang, Y. Zhang, Single-atom engineering to ignite 2D transition metal dichalcogenide based catalysis: fundamentals, progress, and beyond, Chem. Rev. 122 (2022) 1273–1348.

[39] Z.W. Seh, J. Kibsgaard, C.F. Dickens, I. Chorkendorff, J.K. Nørskov, T.F. Jaramillo, Combining theory and experiment in electrocatalysis: Insights into materials design, Science 355 (2017) eaad4998.

[40] F.A. Kröger, H.J. Vink, Relations between the concentrations of imperfections in crystalline solids, in: F. Seitz, D. Turnbull (Eds.) Solid State Physics, Academic Press, 1956, 307-435.

[41] S. He, H. Du, K. Wang, Q. Liu, J. Sun, Y. Liu, Z. Du, L. Xie, W. Ai, W. Huang, Low-temperature molten salt synthesis of MoS2@CoS2 heterostructures for efficient hydrogen evolution reaction, Chem. Commun. 56 (2020) 5548–5551.

[42] C. Wang, B. Tian, M. Wu, J. Wang, Revelation of the excellent intrinsic activity of MoS2|NiS|MoO3 nanowires for hydrogen evolution reaction in alkaline medium, ACS Appl. Mater. Interfaces 9 (2017) 7084–7090.

[43] S.D. Kelly, D. Hesterberg, B. Ravel, Analysis of soils and minerals using X-ray absorption spectroscopy, Methods of Soil Analysis Part 5—Mineralogical Methods (2008) 387–463.

[44] J.H. Lee, S. Kattel, Z. Jiang, Z. Xie, S. Yao, B.M. Tackett, W. Xu, N.S. Marinkovic, J.G. Chen, Tuning the activity and selectivity of electroreduction of CO2 to synthesis gas using bimetallic catalysts, Nat. Commun. 10 (2019) 3724.

[45] G. Kresse, J. Furthmüller, Efficiency of ab-initio total energy calculations for metals and semiconductors using a plane-wave basis set, Comput. Mater. Sci. 6 (1996) 15–50.

[46] G. Kresse, J. Hafner, Ab initio molecular dynamics for liquid metals, Phys. Rev. B 47 (1993) 558–561.

[47] G. Kresse, J. Furthmüller, Efficient iterative schemes for ab initio total-energy calculations using a plane-wave basis set, Phys. Rev. B 54 (1996) 11169–11186.

[48] J.P. Perdew, K. Burke, M. Ernzerhof, Generalized gradient approximation made simple, Phys. Rev. Lett. 77 (1996) 3865–3868.

[49] P.E. Blöchl, Projector augmented-wave method, Phys. Rev. B 50 (1994) 17953–17979.

[50] S. Grimme, J. Antony, S. Ehrlich, H. Krieg, A consistent and accurate ab initio parametrization of density functional dispersion correction (DFT-D) for the 94 elements H-Pu, J. Chem. Phys. 132 (2010) 154104.

[51] X. Qian, J. Liu, L. Fu, J. Li, Quantum spin Hall effect in two-dimensional transition metal dichalcogenides, Science 346 (2014) 1344–1347.

[52] M. Calandra, Chemically exfoliated single-layer ${\text{MoS}}_{2}$: stability, lattice dynamics, and catalytic adsorption from first principles, Phys. Rev. B 88 (2013) 245428.

[53] X. Guo, E. Song, W. Zhao, S. Xu, W. Zhao, Y. Lei, Y. Fang, J. Liu, F. Huang, Charge self-regulation in 1T'''-MoS2 structure with rich S vacancies for enhanced hydrogen evolution activity, Nat. Commun. 13 (2022) 5954.

[54] H.L. Zhuang, M.D. Johannes, A.K. Singh, R.G. Hennig, Doping-controlled phase transitions in single-layer ${\mathrm{MoS}}_{2}$, Phys. Rev. B 96 (2017) 165305.

[55] D.J. Chadi, Special points for Brillouin-zone integrations, Phys. Rev. B 16 (1977) 1746–1747.

[56] J.K. Nørskov, J. Rossmeisl, A. Logadottir, L. Lindqvist, J.R. Kitchin, T. Bligaard, H. Jónsson, Origin of the overpotential for oxygen reduction at a fuel-cell cathode, J. Phys. Chem. B 108 (2004) 17886–17892.

[57] G. Henkelman, B.P. Uberuaga, H. Jónsson, A climbing image nudged elastic band method for finding saddle points and minimum energy paths, J. Chem. Phys. 113 (2000) 9901–9904.

[58] H.M. Jeong, H. Kwon, J.H. Won, Y. Lum, M.-J. Cheng, K.H. Kim, M. Head-Gordon, J.K. Kang, Atomic-scale spacing between copper facets for the electrochemical reduction of carbon dioxide, Adv. Energy Mater. 10 (2020) 1903423.

[59] M.K. Kim, H. Lee, J.H. Won, W. Sim, S.J. Kang, H. Choi, M. Sharma, H.-S. Oh, S. Ringe, Y. Kwon, H.M. Jeong, Design of less than 1 nm scale spaces on SnO2 nanoparticles for high-performance electrochemical CO2 reduction, Adv. Funct. Mater. 32 (2022) 2107349.

[60] C.D. Quilty, L.M. Housel, D.C. Bock, M.R. Dunkin, L. Wang, D.M. Lutz, A. Abraham, A.M. Bruck, E.S. Takeuchi, K.J. Takeuchi, A.C. Marschilok, Ex situ and Operando XRD and XAS analysis of MoS2: a lithiation study of bulk and nanosheet materials, ACS Appl. Energy Mater. 2 (2019) 7635–7646.

[61] T. Stephenson, Z. Li, B. Olsen, D. Mitlin, Lithium ion battery applications of molybdenum disulfide (MoS2) nanocomposites, Energy Environ. Sci. 7 (2014) 209–231.

[62] H. Yu, C. Zhu, K. Zhang, Y. Chen, C. Li, P. Gao, P. Yang, Q. Ouyang, Three-dimensional hierarchical MoS2 nanoflake array/carbon cloth as high-performance flexible lithium-ion battery anodes, J. Mater. Chem. A 2 (2014) 4551–4557.

[63] H. Reddy Inta, T. Biswas, S. Ghosh, R. Kumar, S. Kanti Jana, V. Mahalingam, Ionic liquid-intercalated metallic MoS2 as a superior electrode for energy storage applications, ChemNanoMat 6 (2020) 685–695.

[64] T. Xiang, Q. Fang, H. Xie, C. Wu, C. Wang, Y. Zhou, D. Liu, S. Chen, A. Khalil, S. Tao, Q. Liu, L. Song, Vertical 1T-MoS2 nanosheets with expanded interlayer spacing edged on a graphene frame for high rate lithium-ion batteries, Nanoscale 9 (2017) 6975–6983.

[65] J. He, G. Hartmann, M. Lee, G.S. Hwang, Y. Chen, A. Manthiram, Freestanding 1T MoS2/graphene heterostructures as a highly efficient electrocatalyst for lithium polysulfides in Li–S batteries, Energy Environ. Sci. 12 (2019) 344–350.

[66] L. Wang, X. Zhang, Y. Xu, C. Li, W. Liu, S. Yi, K. Wang, X. Sun, Z.-S. Wu, Y. Ma, Tetrabutylammonium-intercalated 1T-MoS2 nanosheets with expanded interlayer spacing vertically coupled on 2D delaminated MXene for high-performance lithium-ion capacitors, Adv. Funct. Mater. 31 (2021) 2104286.

[67] Y. Li, K. Chang, Z. Sun, E. Shangguan, H. Tang, B. Li, J. Sun, Z. Chang, Selective preparation of 1T- and 2H-phase MoS2 nanosheets with abundant monolayer structure and their applications in energy storage devices, ACS Appl. Energy Mater. 3 (2020) 998–1009.

[68] Z. Xia, Y. Tao, Z. Pan, X. Shen, Enhanced photocatalytic performance and stability of 1T MoS2 transformed from 2H MoS2 via Li intercalation, Results Phys. 12 (2019) 2218–2224.

[69] Z. Sun, L. Lin, M. Yuan, H. Yao, Y. Deng, B. Huang, H. Li, G. Sun, J. Zhu, Mott–Schottky heterostructure induce the interfacial electron redistribution of MoS2 for boosting pH-universal hydrogen evolution with Pt-like activity, Nano Energy 101 (2022) 107563.

[70] Y. Zhang, Y. Kuwahara, K. Mori, C. Louis, H. Yamashita, Hybrid phase 1T/2H-MoS2 with controllable 1T concentration and its promoted hydrogen evolution reaction, Nanoscale 12 (2020) 11908–11915.

[71] W. Chen, J. Gu, Q. Liu, R. Luo, L. Yao, B. Sun, W. Zhang, H. Su, B. Chen, P. Liu, D. Zhang, Quantum dots of 1T phase transitional metal dichalcogenides generated via electrochemical Li intercalation, ACS Nano 12 (2018) 308–316.

[72] M. Acerce, D. Voiry, M. Chhowalla, Metallic 1T phase MoS2 nanosheets as supercapacitor electrode materials, Nat. Nanotechnol. 10 (2015) 313–318.

[73] R. Zhou, S. Yang, T.E.L. Liu, J. Qian, The defect is perfect: MoS2/TiO2 modified with unsaturated Mo vacancies to construct Z-scheme heterojunction & improve mobility of e, J. Clean. Prod. 337 (2022) 130511.

[74] C. Liu, J. Ma, F.-J. Zhang, Y.-R. Wang, C. Kong, Facile formation of Mo-vacancy defective MoS2/CdS nanoparticles enhanced efficient hydrogen production, Colloids Surf. A Physicochem. Eng. Asp. 643 (2022) 128743.

[75] G. Gao, Y. Jiao, F. Ma, Y. Jiao, E. Waclawik, A. Du, Charge mediated semiconducting-to-metallic phase transition in molybdenum disulfide monolayer

and hydrogen evolution reaction in new 1T′ phase, J. Phys. Chem. C. 119 (2015) 13124–13128.

[76] X. Zang, Y. Qin, T. Wang, F. Li, Q. Shao, N. Cao, 1T/2H mixed phase MoS2 nanosheets integrated by a 3D nitrogen-doped graphene derivative for enhanced electrocatalytic hydrogen evolution, ACS Appl. Mater. Interfaces 12 (2020) 55884–55893.

[77] C. Peng, G. Luo, J. Zhang, M. Chen, Z. Wang, T.-K. Sham, L. Zhang, Y. Li, G. Zheng, Double sulfur vacancies by lithium tuning enhance CO2 electroreduction to n-propanol, Nat. Commun. 12 (2021) 1580.

[78] S. Geng, W. Yang, Y. Liu, Y. Yu, Engineering sulfur vacancies in basal plane of MoS2 for enhanced hydrogen evolution reaction, J. Catal. 391 (2020) 91–97.

[79] L. Wu, A. Longo, N.Y. Dzade, A. Sharma, M.M.R.M. Hendrix, A.A. Bol, N.H. de Leeuw, E.J.M. Hensen, J.P. Hofmann, The origin of high activity of amorphous MoS2 in the hydrogen evolution reaction, ChemSusChem 12 (2019) 4383–4389.

[80] L. Zhang, D. Sun, J. Kang, J. Feng, H.A. Bechtel, L.-W. Wang, E.J. Cairns, J. Guo, Electrochemical reaction mechanism of the MoS2 electrode in a lithium-ion cell revealed by in situ and operando X-ray absorption spectroscopy, Nano Lett. 18 (2018) 1466–1475.

[81] N. Rohaizad, C.C. Mayorga-Martinez, Z. Sofer, M. Pumera, 1T-phase transition metal dichalcogenides (MoS2, MoSe2, WS2, and WSe2) with FAst Heterogeneous Electron Transfer: Application on Second-generation Enzyme-based Biosensor, ACS Appl. Mater. Interfaces 9 (2017) 40697–40706.

[82] T.A.J. Loh, D.H.C. Chua, A.T.S. Wee, One-step synthesis of few-layer WS2 by pulsed laser deposition, Sci. Rep. 5 (2015) 18116.

[83] Q. He, L. Wang, K. Yin, S. Luo, Vertically aligned ultrathin 1T-WS2 nanosheets enhanced the electrocatalytic hydrogen evolution, Nanoscale Res. Lett. 13 (2018) 167.

[84] T. Shinagawa, A.T. Garcia-Esparza, K. Takanabe, Insight on Tafel slopes from a microkinetic analysis of aqueous electrocatalysis for energy conversion, Sci. Rep. 5 (2015) 13801.

[85] H. Prats, K. Chan, The determination of the HOR/HER reaction mechanism from experimental kinetic data, Phys. Chem. Chem. Phys. 23 (2021) 27150–27158.

[86] Y. Huang, R.J. Nielsen, W.A. Goddard, III, M.P. Soriaga, The reaction mechanism with free energy barriers for electrochemical dihydrogen evolution on MoS2, J. Am. Chem. Soc. 137 (2015) 6692–6698.

[87] J.K. Nørskov, T. Bligaard, A. Logadottir, J.R. Kitchin, J.G. Chen, S. Pandelov, U. Stimming, Trends in the exchange current for hydrogen evolution, J. Electrochem. Soc. 152 (2005) J23.

[88] J. Wang, K. Chang, Z. Sun, J.H. Lee, B.M. Tackett, C. Zhang, J.G. Chen, C.-J. Liu, A Combined experimental and theoretical study of the accelerated hydrogen evolution kinetics over wide pH range on porous transition metal doped tungsten phosphide electrocatalysts, Appl. Catal. B Environ. 251 (2019) 162–167.

[89] Z. Huang, J. Liu, Z. Xiao, H. Fu, W. Fan, B. Xu, B. Dong, D. Liu, F. Dai, D. Sun, A MOF-derived coral-like NiSe@NC nanohybrid: an efficient electrocatalyst for the hydrogen evolution reaction at all pH values, Nanoscale 10 (2018) 22758–22765.

[90] Y. Xu, S. Yin, C. Li, K. Deng, H. Xue, X. Li, H. Wang, L. Wang, Low-ruthenium-content NiRu nanoalloys encapsulated in nitrogen-doped carbon as highly efficient and pH-universal electrocatalysts for the hydrogen evolution reaction, J. Mater. Chem. A 6 (2018) 1376–1381.

[91] D. Wang, Q. Li, C. Han, Z. Xing, X. Yang, Single-atom ruthenium based catalyst for enhanced hydrogen evolution, Appl. Catal. B Environ. 249 (2019) 91–97.

[92] K. Wu, K. Sun, S. Liu, W.-C. Cheong, Z. Chen, C. Zhang, Y. Pan, Y. Cheng, Z. Zhuang, X. Wei, Y. Wang, L. Zheng, Q. Zhang, D. Wang, Q. Peng, C. Chen, Y. Li, Atomically dispersed Ni–Ru–P interface sites for high-efficiency pH-universal electrocatalysis of hydrogen evolution, Nano Energy 80 (2021) 105467.

[93] Y.-Y. Ma, C.-X. Wu, X.-J. Feng, H.-Q. Tan, L.-K. Yan, Y. Liu, Z.-H. Kang, E.-B. Wang, Y.-G. Li, Highly efficient hydrogen evolution from seawater by a low-cost and stable CoMoP@C electrocatalyst superior to Pt/C, Energy Environ. Sci. 10 (2017) 788–798.

[94] B. Lai, S.C. Singh, J.K. Bindra, C.S. Saraj, A. Shukla, T.P. Yadav, W. Wu, S. A. McGill, N.S. Dalal, A. Srivastava, C. Guo, Hydrogen evolution reaction from bare and surface-functionalized few-layered MoS2 nanosheets in acidic and alkaline electrolytes, Mater. Today Chem. 14 (2019) 100207.

[95] E. Bus, J.A. van Bokhoven, Hydrogen chemisorption on supported platinum, gold, and platinum–gold-alloy catalysts, Phys. Chem. Chem. Phys. 9 (2007) 2894–2902.

[96] M.K. Oudenhuijzen, J.H. Bitter, D.C. Koningsberger, The nature of the Pt−H bonding for strongly and weakly bonded hydrogen on platinum. A XAFS spectroscopy study of the Pt−H antibonding shaperesonance and Pt−H EXAFS, J. Phys. Chem. B 105 (2001) 4616–4622.

[97] O.S. Alexeev, F. Li, M.D. Amiridis, B.C. Gates, Effects of adsorbates on supported platinum and iridium clusters: characterization in reactive atmospheres and during alkene hydrogenation catalysis by X-ray absorption spectroscopy, J. Phys. Chem. B 109 (2005) 2338–2349.

[98] W. Zhao, J. Pan, Y. Fang, X. Che, D. Wang, K. Bu, F. Huang, Metastable MoS2: crystal structure, electronic band structure, synthetic approach and intriguing physical properties, Chem. Eur. J. 24 (2018) 15942–15954.